Arbitrary Lagrangian Eulerian Simulations of High Speed Particle Impacts Encountered During Hypersonic Flight

Peter T. Yip*, Erik Torres*, Ioannis Nompelis*, Thomas E. Schwartzentruber*, Austin J. Andrews**, Devin AJ McGee**, Ioannis Pothos**, Nathan A. Bellefeuille**, Christopher J. Hogan** and David C. Eder***

* Department of Aerospace Engineering and Mechanics, University of Minnesota, Minneapolis, MN, USA.

** Department of Mechanical Engineering, University of Minnesota, Minneapolis, MN, USA.

*** University of Hawai'i at Manōa, USA.

Abstract: Particulate matter and small debris present in the atmosphere are known to cause substantial progressive damage to leading edges and control surfaces on hypersonic vehicles. This study seeks to predict the material responses (mechanical and thermal) to high-speed, small particle impact loading during hypersonic flight. To address such challenges, a multi-material fluid-based approach for modeling problems in this regime is examined. This method combines Arbitrary Lagrangian Eulerian (ALE) hydrodynamics with Adaptive Mesh Refinement (AMR) and multizone physics. The parameter regime of particles (2-5 μm) impacting a material surface at high speeds (125 - 600 ms^{-1}) is investigated.

Keywords: Numerical Algorithms, Computational Fluid Dynamics, Hypersonics, Impact Mechanics, Shock Physics, Arbitrary Eulerian Lagrangian.

1 Introduction

High-speed flight vehicles are continuously challenged to maintain superior flight performance given the most demanding trajectories. One major concern is the cumulative damage on exposed surfaces from flying into small debris, such as rain, ice, sand, ash, etc., at hypersonic velocities. This study seeks to investigate crater formation due to small particle impacts at high velocities. An ALE hydrocode called PISALE (Pacific Island Structured-AMR with ALE) is used to characterize such high-speed impact events to gain an increased understanding of progressive material failure due to particle impingement. The initial studies presented investigate the parameter regimes and material models for an ALE-AMR method to be used to predict the behavior of materials subjected to spherical particle impacts at velocities ranging from 125 - $600 \ ms^{-1}$. The ALE-AMR simulations are compared with experimental characterization of controlled-size particle impacts with surfaces in the same velocity range, to understand the parameters necessary for the eventual development of truly predictive simulations. Future efforts will include material model development and improvement, along with further impingement configurations.

2 Methods

2.1 The PISALE Code

PISALE is an adaptive mesh refinement (AMR)-capable, Arbitrary Lagrangian-Eulerian (ALE) hydrocode developed by the University of Hawai'i [1] (see also https://pisale.bitbucket.io/). The code is described in detail elsewhere, here we give some highlights. To avoid odd-even grid oscillations, the code implements a

structured, staggered grid formulation that computes kinematic variables, namely position and velocity, at the nodes of the computational mesh while kinetic and thermodynamic variables, namely density, internal energy, temperature, pressure, strain, and stress, are computed at the cell-centers and includes models for surface tension effects [2].

The governing fluid equations that PISALE solves are in a Lagrangian formulation (in both vector and index notation i, j, k = 1, 2, 3)

$$\frac{D\rho}{Dt} = -\rho \nabla \cdot \vec{U} = -\rho U_{i,i} \tag{1}$$

$$\frac{D\vec{U}}{Dt} = \frac{1}{\rho} \nabla \cdot \boldsymbol{\sigma} = \frac{1}{\rho} \sigma_{ij,j} \tag{2}$$

$$\frac{De}{Dt} = \frac{1}{\rho} V \mathbf{s} : \dot{\mathbf{\epsilon}} - P\dot{V} = \frac{1}{\rho} V(s_{ij}\dot{\mathbf{\epsilon}}_{ij}) - P\dot{V}$$
(3)

where ρ is the density, $\vec{U} = (u, v, w)$ is the material velocity, t is time, $\boldsymbol{\sigma}$ is the total stress tensor, P is the pressure, e is the total internal energy, V is the relative volume ($\rho V = \rho_0$ where ρ_0 is the reference density), \boldsymbol{s} is the deviatoric stress, and $\dot{\boldsymbol{\epsilon}}$ is the strain rate tensor.

Thermodynamic quantities are determined from a pressure equation of state (EOS), which evaluates pressure as a function of density and internal energy/temperature. PISALE can use a tabulated EOS to obtain an equation of state for a given material, or a user-defined functional EOS can be developed as needed. The deviatoric stresses are determined by a constitutive relation derived from the flow stress model implemented.

The numerical algorithm begins with an explicit time-marching Lagrange step. Explicit time-marching refers to the use of previous time step values to compute current time step values. A Lagrange step refers to $\frac{D}{Dt} = \frac{\partial}{\partial t}$ meaning that the mesh and material nodes deforms together i.e., the advection term within the material derivative is not computed. Following the explicit Lagrange step, the remap step determines where the new grid node positions will go. To emulate a purely Eulerian method with the Lagrangian formulation, the grid nodes can be remapped back to the original grid location at the start of the simulation. In a pure Lagrangian scheme, the grid nodes and material nodes are in the same position for the next time step, and there is no need to remap. However, it is the remap step that gives ALE its greatest strength [3]. The algorithm is provided criteria that will remap the grid nodes typically somewhere in-between the mesh at the beginning of the Lagrange step and the deformed mesh at the end of the Lagrange step. ALE methods are often used to prevent mesh tangling issues. It is often preferred for dynamic impact simulations to stay in the Lagrangian scheme until the grid deforms too severely such that remapping grid nodes is required to alleviate grid distortion limits, consequently requiring to advect quantities across faces of the prior mesh to the remapped mesh. In PISALE, there is increased modularity that allows the user to include an Operator Split step following the Remap step that can include additional physics such as, heat conduction, radiation transport, and surface tension. The final step in the algorithm is the AMR step that marks zones for refinement/de-refinement, groups refinement operations in patches with minimum number of zones, and creates and transfers new grid hierarchy to the newly refined state.

2.2 2D Axisymmetric Simulation Setup

The experimental configuration consists of small, spherical, aluminum 6061-T6 projectiles impacting sufficiently thick, cylindrical, aluminum 6061-T6 plates at varying impact velocities. We use a surogate material for the EOS for aluminum 6061-T6 in the simulations. All simulations use a 90° angle of incidence relative to the target plate and take advantage of cylindrical symmetry of the configurations.

Material	A [MPa]	B [MPa]	С	n	m
Aluminum 6061-T6	324	114	0.002	0.42	1.34

Table 1: Johnson-Cook Flow Stress Model Material Parameters for Aluminum 6061-T6 [4]

Material	D_1	D_2	D_3	D_4	D_5	$T_{room}[C^{\circ}]$	$T_{melt}[C^{\circ}]$
Aluminum 6061-T6	-0.77	1.45	-0.47	0.0	1.34	20	650

Table 2: Johnson-Cook Damage Model Material Constants for Aluminum 6061-T6 [4]

Material	σ_{yield} [MPa]	Shear Modulus [MPa]	T_{melt} [K]	Spall Strength [MPa]
Aluminum 6061-T6	324	26,000	925	10,000

Table 3: Additional material parameters for aluminum 6061-T6 required for fully defining a material in PISALE [4]

The physical dimensions of the simulation domain are $L_x \times L_y = 100.0 \mu m \times 100.0 \mu m$ with the axis of symmetry along the x-axis. The target plate dimensions for all simulations are set to $75.0 \mu m \times 100.0 \mu m$ while the projectile diameters are varied between two values: $2.0 \mu m$ and $5.0 \mu m$. The target plate dimensions are significantly larger than the projectile size to ignore stress wave reflections from the outer surfaces where symmetry boundary conditions i.e. zero gradients are applied. Initial grid spacing was set to $0.5 \mu m$ in x-and y- directions with the smallest (automatic) refinement grid size being 50nm. The global time step was kept at PISALE's maximum value of $\delta t = 1.0 \times 10^{-6}$ with a CFL set to 0.4. The simulation end time is set to $t_{end} = 0.01 \mu s$ and was pre-determined by a calculation of when the interface velocity between the projectile and target should reach zero velocity. Figure 3 illustrates that the interface velocity comes to full rest at around 5ns, which is lower than predicted.

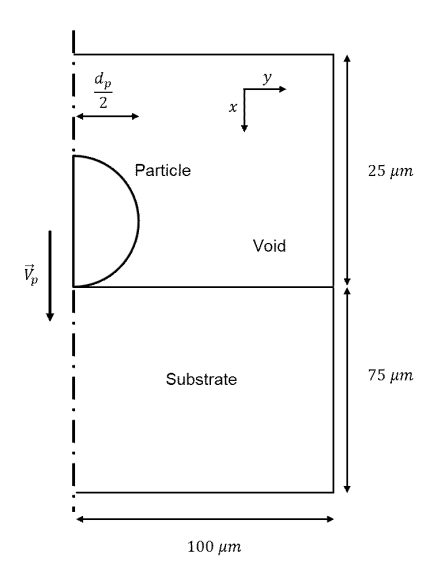


Figure 1: Diagram of simulation domain employed wherein spherical particles with an initial velocity $(\vec{V_p})$ are placed in direct contact with substrate surface. Overall domain dimensions are 100 μm by 100 μm with a substrate thickness of 75 μm .

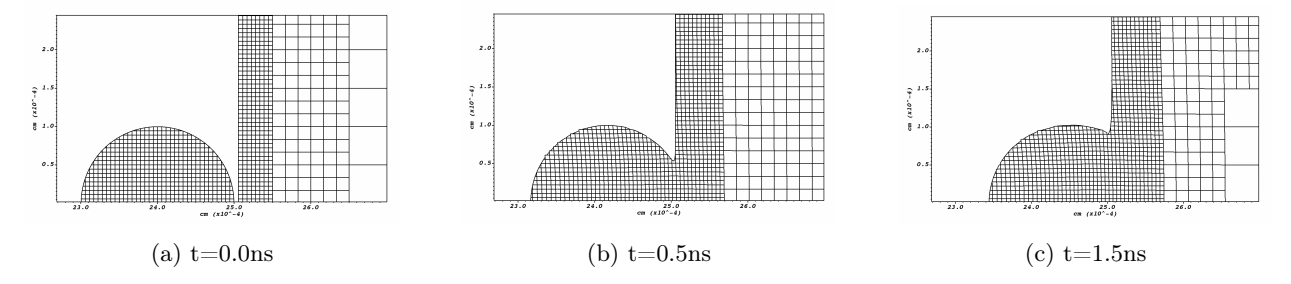


Figure 2: Mesh quality and reconstruction near the particle surface interface at 0, 0.5 and 1.5 ns of simulation time for 2 μm diameter particle with an initial velocity of 325 ms^-1 and density of 2.7 gcm^-3 .

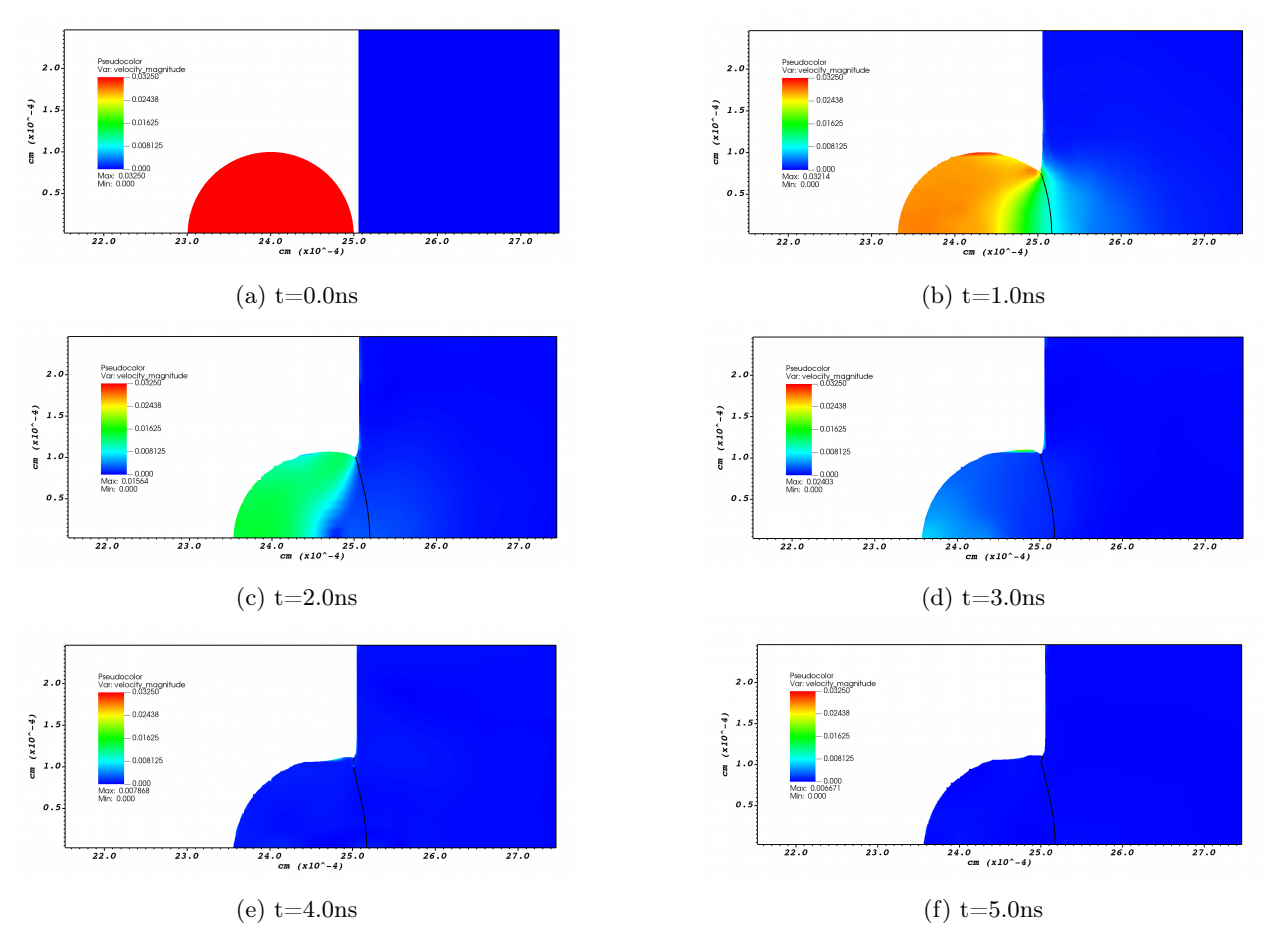


Figure 3: Velocity magnitude at different time intervals

PISALE requires six material models to fully define any material used in the simulation.

- 1. Equation of State
- 2. Shear Modulus Model
- 3. Melt Model
- 4. Flow Stress Model
- 5. Spall Strength Model
- 6. Failure/Damage Model

Tabulated values are used to approximate the equation of state for the Aluminum 6061-T6, while the shear modulus, melt temperature, and spall strength are set as constants through the entire simulation time. Values for the material constants are shown in Table 3. The Johnson-Cook flow stress and damage model are used for both projectile and target materials with parameters shown in Table 1 and Table 2, respectively. dd A major point of discrepancy in this preliminary study, is that the projectile material used in the simulation is not the same as the material used in the experiments. The material used in the experiments is discussed in Section 2.3 and is a unique material that we do not currently have material model parameters for. However, some prior studies have concluded that the primary material parameter of the projectile that affects penetration depth is its density [5, 6]. Since material data is not available for the projectile used in the experiment, a well-characterized material of similar density to the experimental projectile i.e. aluminum 6061-T6 is used as a surrogate material for the simulations. An additional caveat must be stated, as the statement of projectile parameters affecting penetration depth is predicated on the fact that the code is able to consider elastic rebounding effects. If a number of materials come into contact within a single zone, the zone becomes a mixed cell that contains all materials in contact. PISALE's mixed cell model currently does not permit the separation of materials within the mixed cell and will remain a mixed cell throughout the duration of the simulation. Therefore, only inelastic collisions can be considered and it is hypothesized that the strength of the projectile will be an additional parameter that affects penetration depth due to the additional time the projectile is transferring energy and momentum as opposed to allowing for rebounding effects in the conservation equations. Future work could be dedicated to developing more detailed material models for more accurate comparisons to these particular experiments.

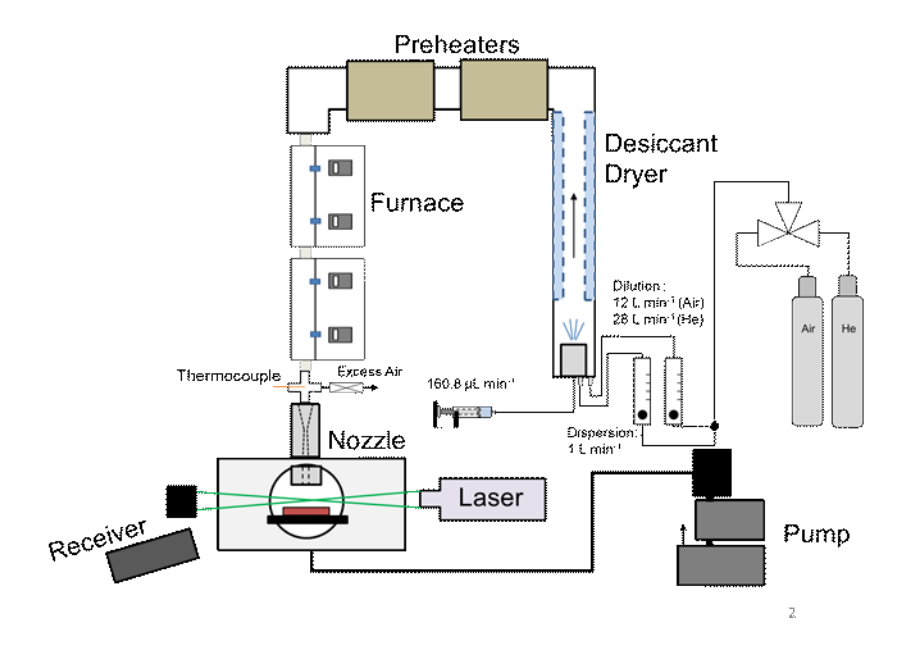
2.3 Experimental Setup

An experimental apparatus shown in Fig. 4 has been designed to generate well characterized spherical monodisperse ferrous sulfate particles that are accelerated and impacted onto polished Aluminum 6061-T6 substrates. Particles with a diameter of 2 (1.9) and 5 (4.9) micrometers are generated using a vibrating orifice aerosol generator (VOAG; Model 3450, TSI inc.) from a solution of ferrous sulfate heptahydrate. These particles are flowed through silica bead dryers to remove any moisture content and form solid ferrous sulfate particles. Particle diameter (d_p) is controlled by varying ferrous sulfate heptahydrate concentrations

 (C_s) , orifice vibration frequency (f) and solution flow rate (Q) using $d_p = \left(\frac{6QC_s}{\pi f}\right)^{\frac{1}{3}}$ from Berglund et al. [7]. The particle size and morphology are measured with both a Aerodynamic Particle sizer, APS (Model 3321, TSI inc), and Scanning Electron microscopy (SEM), refer to Figure 5. After generating and completely drying, the particles are accelerated by a custom converging diverging nozzle with an exit diameter of 2 mm and throat diameter of 1 mm. System velocity is controlled by the upstream temperature and carrier gas which can be either air or helium, or some mixture of both. The impacted surface is placed 2 mm downstream of the nozzle exit. Particle velocities are measured 1 mm downstream of the nozzle exit by laser Doppler velocimetry, LDV model PS-TM-1D-532 TSi inc, with the receiver at a 30 degree forward scatter. The measured velocity is in the range of 300 to 600 ms^{-1} with a distribution width of approximately 50 to 100 ms^{-1} , refer to Figure 6. Velocities reported for each experimental condition and used in comparison to simulation data are the most probabilistic (mode) velocity.

Experiments are conducted with the conditions outlined in Table 4. For each condition outlined, the system is run for 30s to allow for even and independent deposit of the generated particles. Changes in

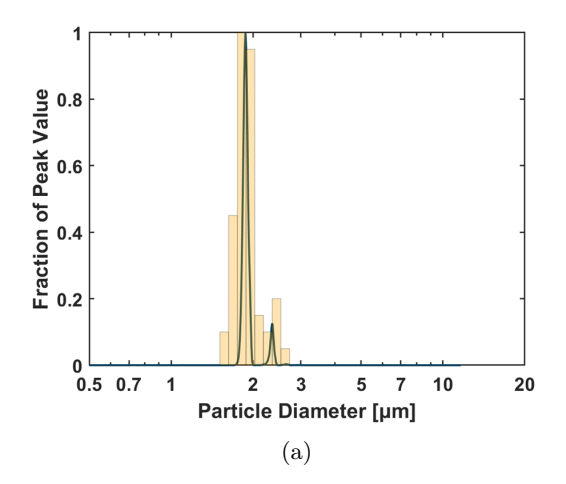
surface topography are measured using tapping mode atomic force microscopy with a Bruker Nanoscop V Dimension ICON. The probes used have a nominal tip diameter of 4 nm (ScanAsyst-Air, Bruker). Multiple independent cratering events are analysed and averaged for each sample with associated 95% confidence intervals.



 $Figure\ 4:\ A\ schematic\ diagram\ of\ monodisperse\ particle\ generation,\ nozzle\ injection\ system\ and\ laser\ Doppler\ velocity\ measurements.$

Table 4: List of experimental conditions

Condition	Gas Composition	$d_p[\mu m]$	$u[\mathrm{km}\;\mathrm{s}^{-1}]$
1	Air	1.9	0.35
2	Air	4.9	0.30
3	Helium	4.9	0.60



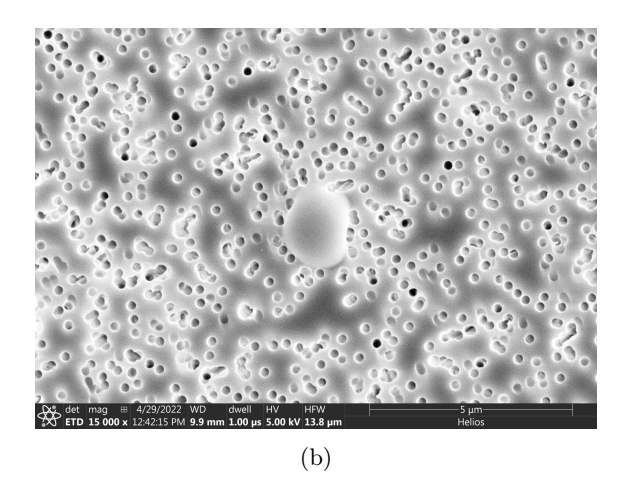


Figure 5: Characterization of generated 2 μm ferrous sulfate particles by APS and SEM. a) Particle size distribution as measured by APS (solid) and SEM (bars). b) Scanning electron microscope image of a 2 μm ferrous sulfate particle collected on a 200 nm pore membrane filter.

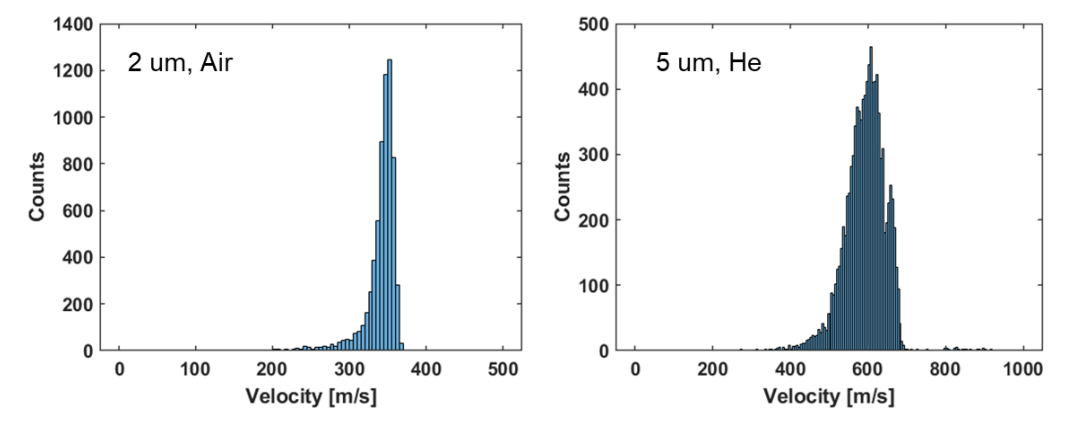


Figure 6: Velocity distribution from a) 2 μm particles being accelerated in Air at STP and b) 5 μm particles accelerated in Helium at STP.

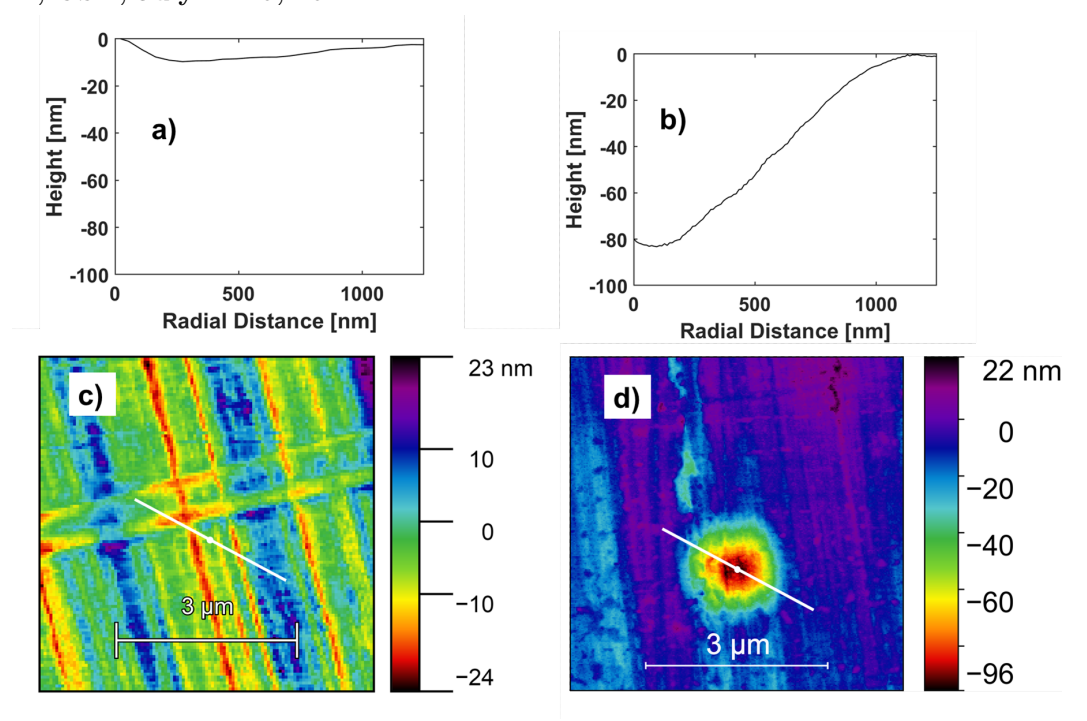


Figure 7: Radially averaged profiles for d) untouched polished surface c) crater formation after 2 μm impact in Air (measured velocity of 350 ms^{-1}) with corresponding Atomic Force Microscopy topographies and radial average origin a) and b).

3 Results

3.1 Theoretical Analysis

A 1D penetration depth analysis presented by Walker is performed for the sphere-plate impact configuration [6]. The impact event is treated as a discontinuous disturbance such that discrete states left and right of the wave can be initially known. This initial value problem (IVP) is known as the Riemann problem. The Rankine-Hugoniot jump conditions represent the locus of states before and after the passing of a discontinuity, therefore, the jump conditions are valid equations that can be applied at each wave represented as a slope, or characteristic, in x-t space. By utilizing the jump conditions to determine state variables left and right of the characteristics, the velocity at the contact interface can be determined since the contact surface requires the velocity and stress must be equal at the point of contact. A similar solution can be performed using the method of characteristics solution to the linear wave equation [8]. The derived interface velocity is given in Eq. 4 and simplified in Eq. 5

$$u = \frac{Z_p}{Z_p + Z_t} u_{imp} \tag{4}$$

$$u = Bu_{imp} \tag{5}$$

where Z_p and Z_t are the acoustic impedances of the projectile and target, respectively, with $Z = \rho U$; U being the wave speed within the material. Assuming a linear stress-strain relationship, the wave speed can be taken as the adiabatic, acoustic sound speed within the material, c.

Since the projectile target material are the same, the velocity equation further reduces to

$$u_{interface} = \frac{1}{2} u_{imp} \tag{6}$$

which provides an easy calculation to compute the velocity experienced in the projectile and target when

they are the same material.

Displacement can then be calculated by multiplying the velocity with the time of impact, $t_{imp} = \frac{2L_p}{c_p}$. The time of impact is the total time for a single wave cycle to propagate through the projectile.

$$\delta_{final} = ut_{imp} = \frac{1}{2}u_{imp}t_{imp} = \frac{u_{imp}}{c_p}L_p \tag{7}$$

Fig. 8 illustrates the computed values of Eq.7 with varying velocities and compared with penetration depths calculated from numerical simulations.

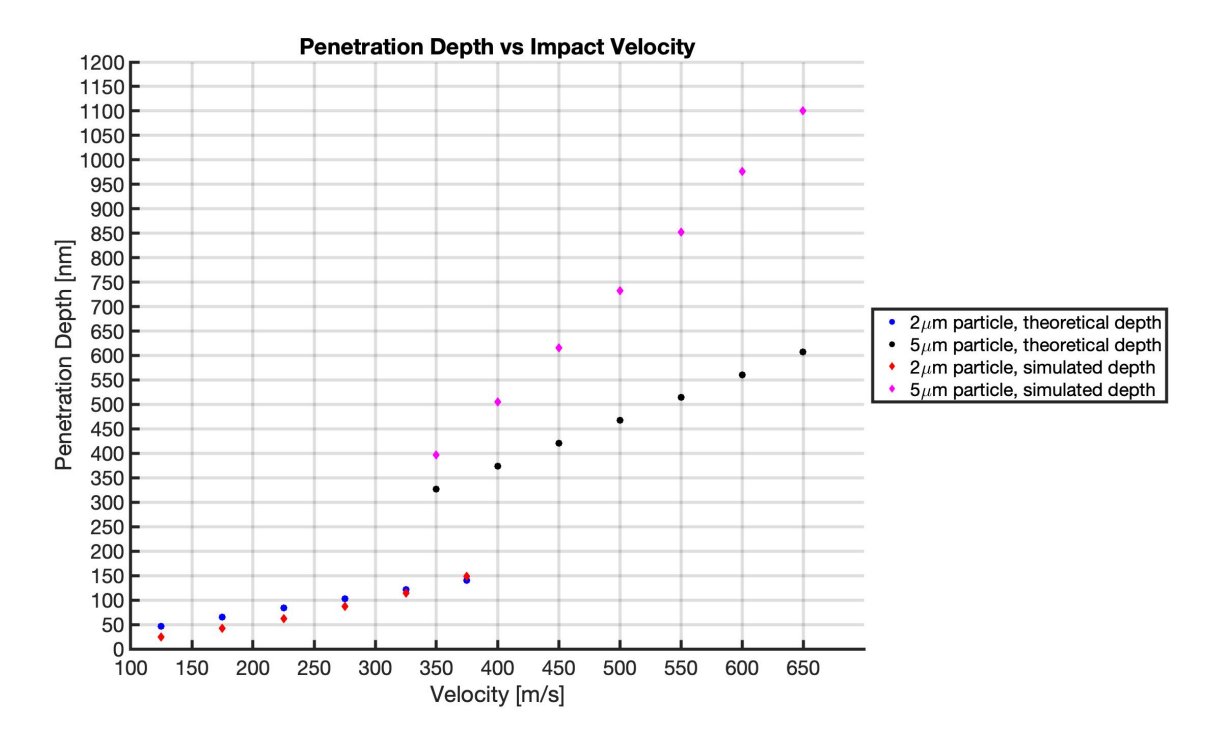


Figure 8: Analytical and simulated penetration depths as a function of impact velocity. This data illustrates a strong agreement with $2\mu m$ particle impacts at lower velocities and poor agreement with $5\mu m$ particle impacts at higher velocities.

The theoretical and simulated predictions prove to have strong agreement for the $2\mu m$ particle at lower velocities. However, there is strong disagreement with the $5\mu m$ particles at higher velocities. It is expected that the analytical approach should agree with the lower velocity cases since the strains experienced are small enough to where small strain, linear elasticity theory is applicable. However, as the velocities increase, consequently the strain rate and kinetic energy increases, which leads to the need for finite strain plasticity theory that the analysis does not account for. The simulation utilizes a strain-rate and temperature dependent flow stress model, therefore, the simulation will take into account more factors of material failure the simple 1D theoretical predictions do not.

3.2 Simulation Results

In this section, the von-Mises stress, temperature, and equivalent plastic strain plots are presented for the impact configurations discussed in Section 2.2. The simulation results shown are with an impact velocity of $325 \ ms^{-1}$ and a projectile diameter of $2\mu m$. PISALE shows a strong ability to capture detailed effects expected in this type of impact event, however, the magnitude of each quantity of interest is an area of continued investigation.

The evolution of the von-Mises stress is shown in Fig.9. At a time of 1 ns, a compression wave propagates immediately into both the projectile and target. An interesting feature of the von-Mises stress snapshot at

1 ns is the non-spherical profile of the propagating wave. A kink is observed in the higher stress regions towards the top of the contact interface. This indicates that the PISALE code does well in capturing the wave transmissions and reflections as a crater crown forms, which is where the kink originates. At 2 ns and 3 ns snapshots, the stress reduces at the back (left side) of the projectile due to the tensile wave reflection that occurs when a compression wave meets a free surface. PISALE also captures this detail well. As the projectile comes to rest, there is residual stress that remains in the target and projectile. The amount of maximum residual stress is about a 12.25% difference from the reported yield stress value shown in Table 1. While this result is within reason, this is a future area of work to discover whether this amount of residual stress is to be expected or not.

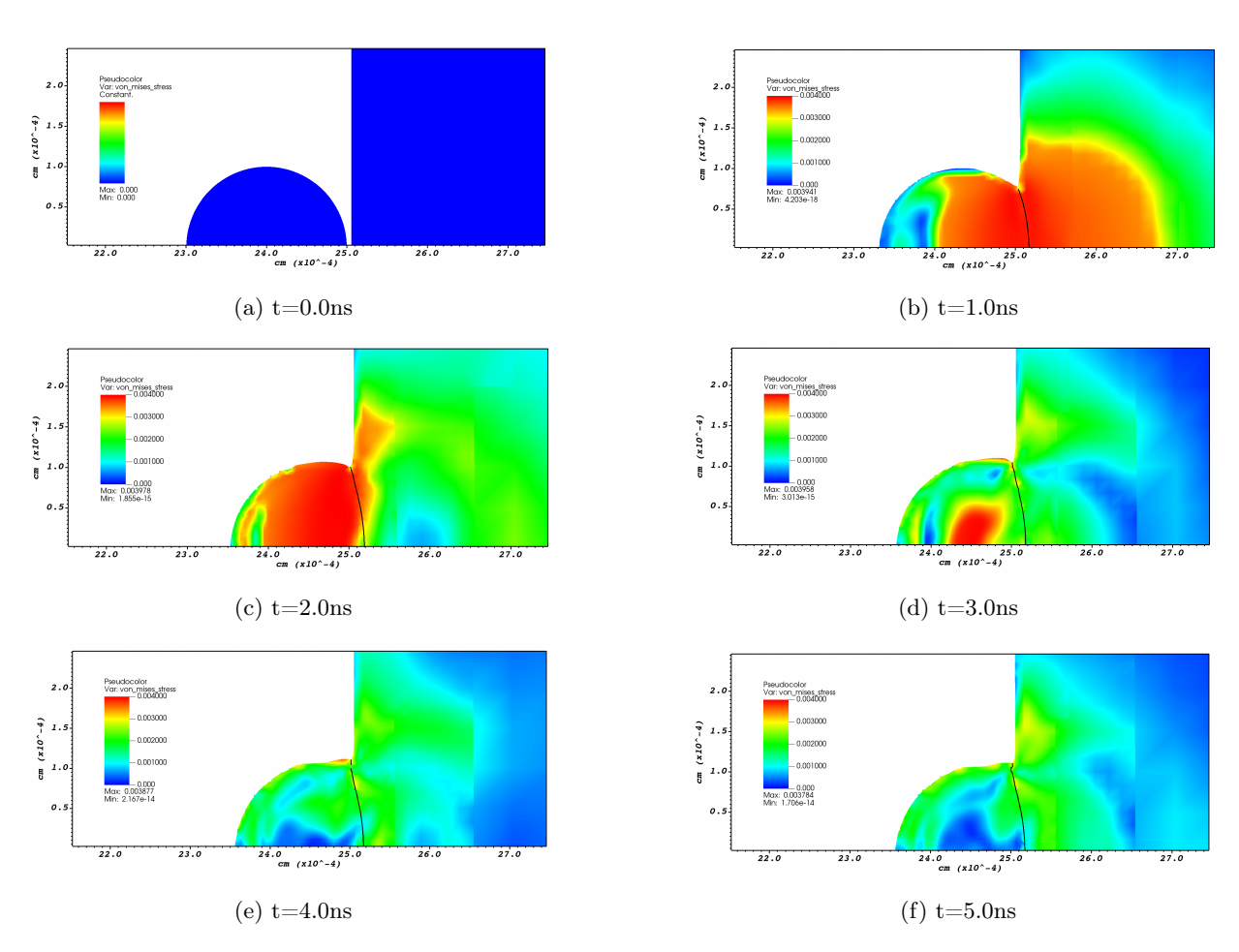


Figure 9: von Mises stress contours for a $325ms^{-1}$ impact of a $2\mu m$ aluminum 6061-T6 projectile on an aluminum 6061-T6 thick plate at different time intervals

The evolution of the temperature distribution is shown in Fig. 10. The results illustrate a localization of higher temperature at the contact interface farthest away from the centerline of impact. Due to the symmetrical nature of the impact configuration, the temperature profile is not expected to be localized at a single location on the contact interface. It is expected that the temperature should be highest and even along the contact interface while having a mirroring gradient in the projectile and target since the materials are the same. Further work may be warranted to determine whether this result is physically accurate.

As a spherical projectile with momentum great enough to invoke plastic instability makes contact with a flat target, the material is radially displaced. Therefore, it is expected that a localization of plastic strain exists towards the outer radius of the projectile-target interface. PISALE captures this phenomena well and is shown in Fig.11 Note that the range of values associated with the colorbar and the contour values change for the different times. While the location of the plastic strain is understood, the net amount of plastic strain

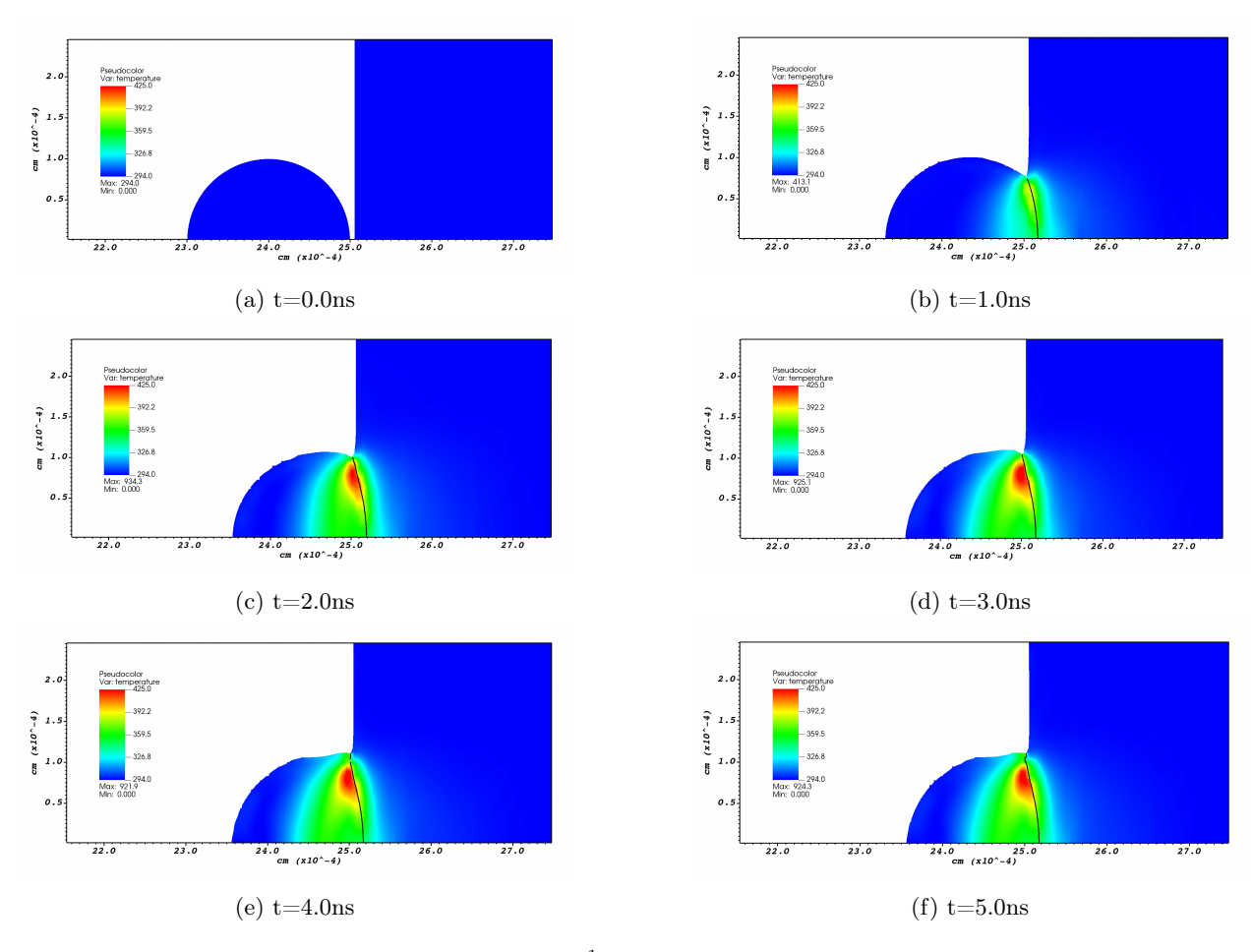


Figure 10: Temperature contours for a $325ms^{-1}$ impact of a $2\mu m$ aluminum 6061-T6 projectile on an aluminum 6061-T6 thick plate at different time intervals in Kelvin

requires further verification.

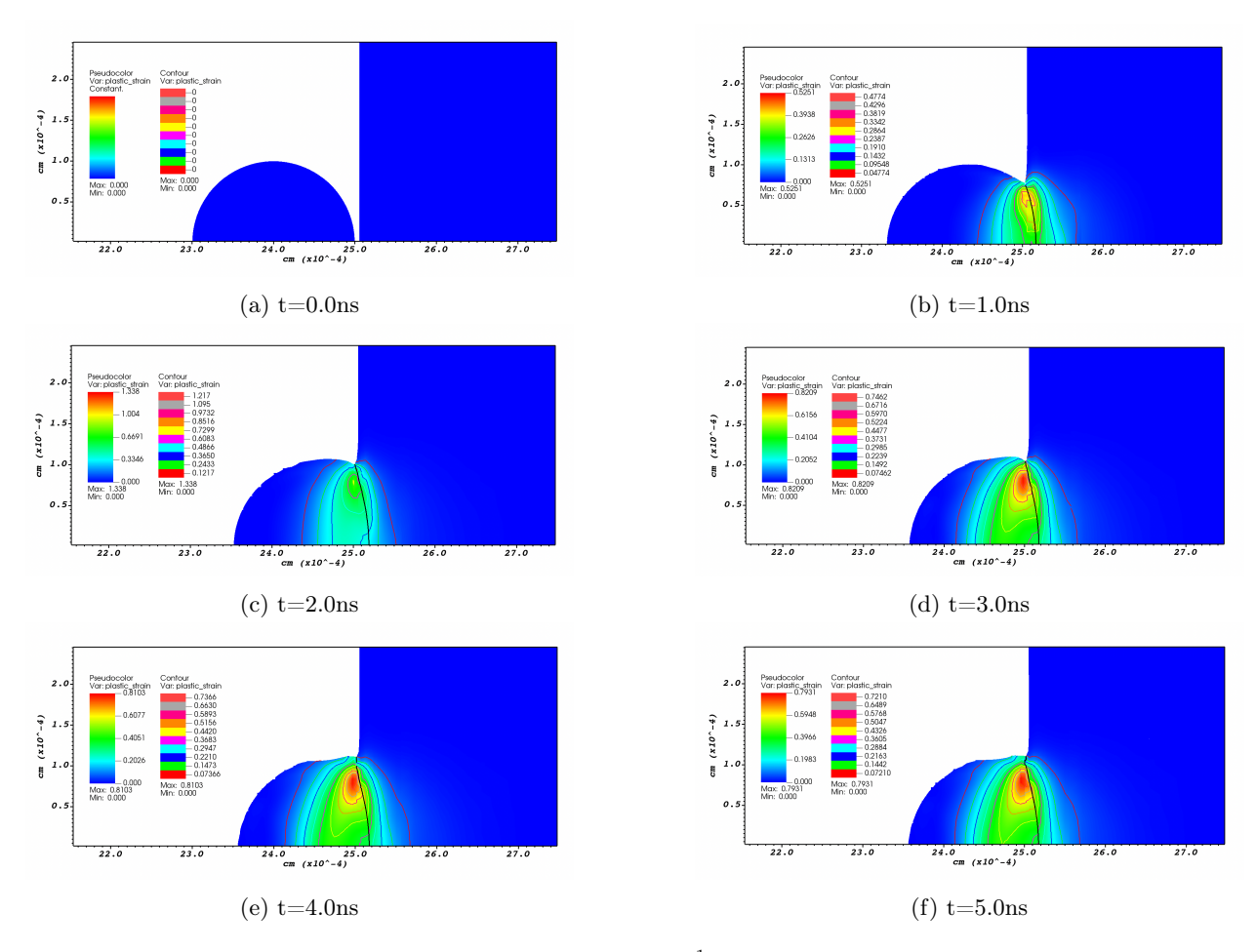


Figure 11: Equivalent plastic strain contours for a $325ms^{-1}$ impact of a $2\mu m$ aluminum 6061-T6 projectile on an aluminum 6061-T6 thick plate at different time intervals

3.3 Experimental Results

The PISALE methodology has been experimentally verified for a wide variety of problems relevant for high speed micrometer particle impacts[9, 10] and experimental/simulation comparisons relevant to high-speed aerospace flows are ongoing. To understand the efficacy of this model, simulations are conducted to match experiments outlined in Table 4.

As shown in simulations, crater formation creates large amounts of surface plastic deformation. Experimentally, this is shown by surface topographies produced from AFM as shown in Figure 8. In this result, a clear and non negligible surface topography change has occurred between the virgin material and a surface that has been treated by high speed particle impacts. To better compare results with simulation data, craters are radially averaged

$$\bar{h}_{\theta}(r) = \frac{1}{2\pi} \int_{0}^{2\pi} h(r,\theta) d\theta \tag{8}$$

where h is the height of the surface, r is the distance from the center of the crater and θ is the azimuthal angle.

For these results, five independent cratering events are found and analyzed to obtain statistical variance on the formed craters. The results of these profiles are then compared to simulation data shown in Fig. 12. The discrepancy between the simulated crater and the experimental results are not explained by the variance in either AFM statistical uncertainty, nor small variations in impacting particle velocity ($\pm 50ms^{-1}$). A clear difference between experiments and simulations are that particles do not retain themselves on the surface of the material unlike in the simulations. Potentially, this is due to the difference in projectiles properties such as indentation hardness or applicability of the material properties and models used in the code. The current simulation models treat the impact as an inelastic collision where plastic deformation occurs in the radial direction. As a consequence, the projectile is able to cause additional material flow in the substrate to generate large embankments or crest features not seen in the experimental data. Finally, in the experiments, as the supersonic jet impinges on the material sample, a shock wave and post-shock low-velocity region of gas is formed above the sample surface. Particle-flow simulations using particle drag models (not described in this paper) show that particles may decelerate in this region by upwards of 100 m/s before impacting the sample. Therefore, it is possible that the impact velocities used in the simulations are upper estimates, which would therefore over-predict the crater depth, as seen in Figure 12. Minimizing such discrepancies between the simulations and experiments will be the focus of future work.

To quantify the substrate material movement, we propose utilizing total crater volume normalized by incident particle volume

$$V^* = 12 \frac{\int_0^{R(h=h_{max})} |h_{max} - \bar{h}_{\theta}(r)| r dr}{d_p^3}$$
 (9)

where R is the location of maximum height, h_{max} the maximum height and d_p is the size of the particle. Results from the experiments and simulation are shown in Fig. 13 along with an empirical crater depth model developed by Price et al for particle impacts onto aluminum 1100 [5]. These results show that there exists a strong power law relationship between the substrate material displaced and kinetic energy

$$V^* = A \left(\frac{1}{2}u^2\right)^{\alpha} \tag{10}$$

where the exponential factor, α , spans from 1 to 2. Future work is required to make definitive conclusions of the physical mechanisms governing this relationship, if one exists at all. However, preliminary conclusions are made by examining the elastic-plastic analysis from Yildirim et al. [11].

Starting with the work-energy principle, the net work done within an object is equivalent to its change in kinetic energy.

$$W_{net} = \frac{1}{2}m(u_{final}^2 - u_{initial}^2) \tag{11}$$

If thermodynamic effects are assumed to have minimal effect to the system, the net work done can be captured solely by strain energy within the material

$$W_{net} = \sum_{i,j=1}^{3} \sigma_{ij} d\epsilon_{ij} \tag{12}$$

Hutchings [12] calculated an empirical strain rate for microparticle impacts on a flat plate to be

$$\dot{\epsilon} \approx 0.2 \left(\frac{u_i^{1/2} H^{1/4}}{\rho^{1/4} r_p} \right) \tag{13}$$

where H is the indentation hardness and r_p is the projectile radius. PISALE is also able to track the strain rate within the objects to verify the validity of this empirical strain rate derivation.

By integrating Eq.13 over the time of impact and substituting into Eq.12, the result can be substituted into Eq.11 to obtain the kinetic energy. The normalized crater volume, V^* can then be measured at each time step and determine if the relationship between kinetic energy and normalized crater volume holds true. The results of these calculations are currently being pursued as future work.

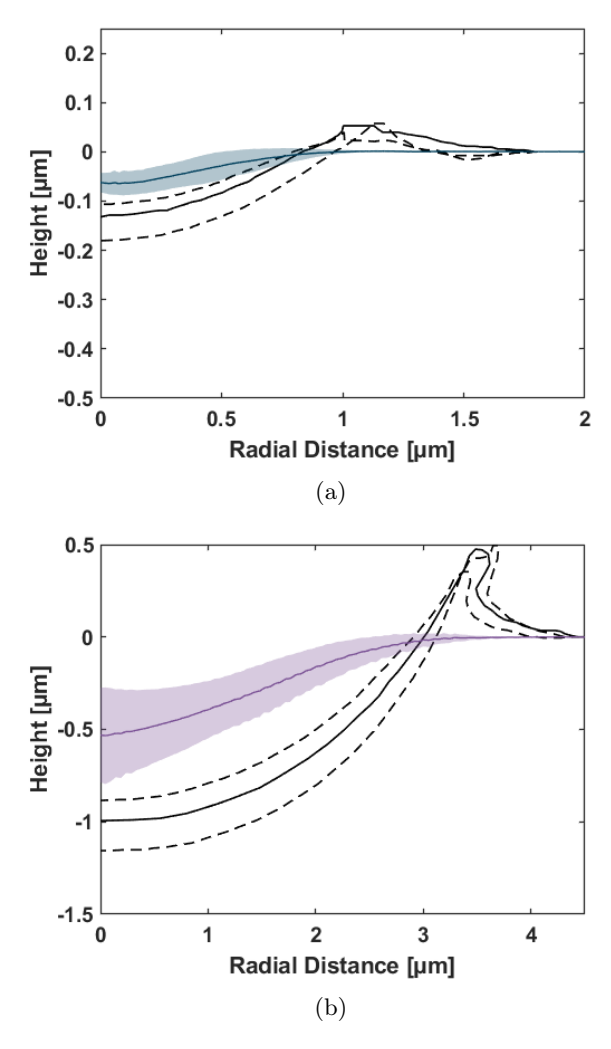


Figure 12: Comparison of radially averaged profiles with associated 95% confidence interval (blue) with simulation data (black) for a) 2um particles impacting at 350 ms^{-1} and b) 5 μm particles impacting at 600 ms^{-1} (purple). Dashed black lines represent simulations run at velocities \pm 50 ms^{-1}

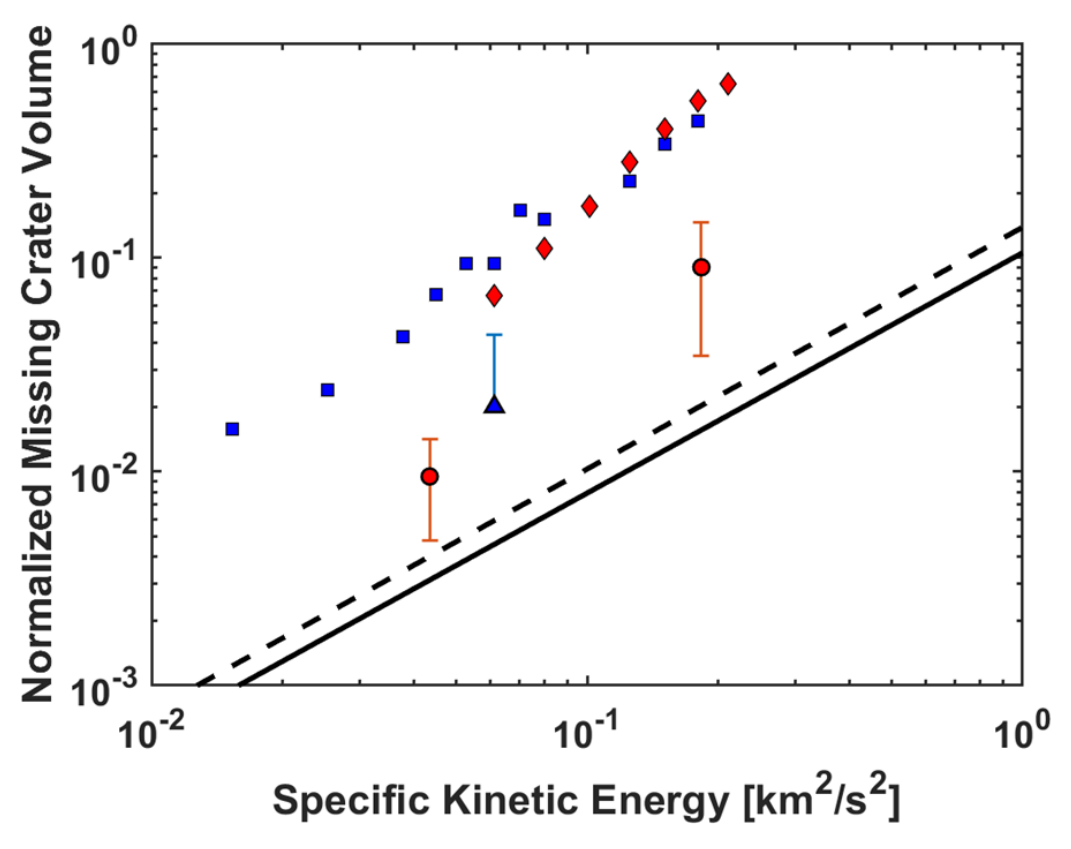


Figure 13: Variation of total crater volume normalized to impacting projectile volume as a function of particle kinetic energy. Experimental data outline in Table 4 are shown with subsequent error bars for projectiles with a diameter of 2 μm impacting at 350 ms^{-1} (blue triangle) and for diameters of 5 μm impacting at 300 ms^{-1} and $600ms^{-1}$ (red circle). Results are compared to simulation data for 2 μm sized particles (red diamonds) and 5 μm sized particles (blue squares) and to Price et al. for 2 μm (solid black) and 5 μm (dashed black).

4 Summary

An evaluation of an ALE-AMR tool for small particle impact mechanics was conducted and simulation results were compared with experiment. Appropriate material models for inclusion in the PISALE framework are studied. Mesh refinement is successful in capturing detailed features such as wave reflections from displaced surfaces at the contact interface, but net values of parameters, such as von-Mises stress, temperature, and equivalent plastic strain, are significantly model dependent. Appropriate EOS values either in tabulated or analytic form and other material models will be required for PISALE to simulate the elastic collision behavior seen in certain experiments, as well as appropriate material models. Continued verification must be completed before such simulations can be considered predictive for these small particle, high-velocity, impact conditions.

5 Acknowledgements

We would like to thank many additional members of the PISALE team for their expertise and assistance throughout all aspects of our study and for their help in writing this manuscript. This research is supported by the Office of Naval Research, under ONR MURI Award Number N00014- 20-1-2682. The PISALE code is supported by the National Science Foundation, under Office of Advanced Cyber Infrastructure Award Number 2005259, the U. S. Department of Energy, Office of Science, under Fusion Energy Sciences Research Division Award Number DE-SC0021374. This research used resources of the National Energy Research Scientific Computing Center (NERSC), a U.S. Department of Energy Office of Science User Facility located at Lawrence Berkeley National Laboratory, operated under Contract No. DE-AC02-05CH11231 using NERSC awards ERCAP0020882 and ERCAP0020890. Parts of this work were carried out in the Characterization Facility, University of Minnesota, which receives partial support from the NSF through the MRSEC (Award Number DMR-2011401) and the NNCI (Award Number ECCS-2025124) programs.

References

- [1] Alice Koniges, Nathan Masters, Aaron Fisher, David Eder, Wangyi Liu, Robert Anderson, David Benson, and Andrea Bertozzi. Multi-material ale with amr for modeling hot plasmas and cold fragmenting materials. *Plasma Science and Technology*, 17(2):117, 2015.
- [2] W. Liu, A. Koniges, K. Gott, and D. Eder. Surface tension models for a multi-material ale code with amr. *Int Computers and Fluids*, 151:91–101, 2017.
- [3] J. A. Zukas. Introduction to Hydrocodes. Elsevier, 2004.
- [4] D. R. Lesuer, G. J. Kay, and M. M. LeBlanc. Modeling large-strain, high rate deformation in metals. *Proceedings of the 3rd Biennial tri-laboratory engineering conference modeling and simulations*, pages 3–5, 1999.
- [5] M. C. Price, A. T. Kearsley, M. J. Burchell, L. E. Howard, J. K. Hillier, N. A. Starkey, P. J. Wozniakiewicz, and M. J. Cole. Stardust interstellar dust calibration: Hydrocode modeling of impacts on al-1100 foil at velocities up to 300kms⁻¹ and validation with experimental data. *Meteorites and Planetary Science*, 47(4):684–695, 2012.
- [6] J. D. Walker. Modern Impact and Penetration Mechanics. Cambridge University Press, 2021.
- [7] Richard N. Berglund and Benjamin Y. H. Liu. Generation of monodisperse aerosol standards. *Environmental Science & Technology*, 7(2):147–153, 1973. PMID: 22224997.
- [8] D. S. Drummheller. Introduction to Wave Propagation in Nonlinear Fluids and Solids. Cambridge University Press, 1998.
- [9] A E Koniges, N D Masters, A C Fisher, R W Anderson, D C Eder, T B Kaiser, D S Bailey, B Gunney, P Wang, B Brown, K Fisher, F Hansen, B R Maddox, D J Benson, M Meyers, and A Geille. ALE-AMR: A new 3d multi-physics code for modeling laser/target effects. *Journal of Physics: Conference Series*, 244(3):032019, 2010.
- [10] D.C. Eder, A.C. Fisher, A.E. Koniges, and N.D. Masters. Modelling debris and shrapnel generation in inertial confinement fusion experiments. *Nuclear Fusion*, 53(11):113037, 2013.

- [11] B. Yildirim, H. Yang, A. Gouldstone, and S. Müftü. Rebound mechanics of micrometre-scale, spherical particles in high-velocity impacts. *Proc. R. Soc. A*, 2017.
- [12] I. Hutchings. Strain rate effects in microparticle impact. J. Phys. D, 10, 1977.